

2

DTIC FILE COPY

MEMORANDUM REPORT BRL-MR-3848

AD-A224 287

**BRL**

DIRECT NUMERICAL SIMULATION  
OF TURBULENT COUETTE FLOW

DTIC  
ELECTE  
JUL 25 1990  
S D  
D CG D

JOHN D. KUZAN  
KURT D. FICKIE

JUNE 1990

APPROVED FOR PUBLIC RELEASE; DISTRIBUTION UNLIMITED.

U.S. ARMY LABORATORY COMMAND

BALLISTIC RESEARCH LABORATORY  
ABERDEEN PROVING GROUND, MARYLAND

## **NOTICES**

Destroy this report when it is no longer needed. DO NOT return it to the originator.

Additional copies of this report may be obtained from the National Technical Information Service, U.S. Department of Commerce, 5285 Port Royal Road, Springfield, VA 22161.

The findings of this report are not to be construed as an official Department of the Army position, unless so designated by other authorized documents.

The use of trade names or manufacturers' names in this report does not constitute indorsement of any commercial product.

## UNCLASSIFIED

## REPORT DOCUMENTATION PAGE

Form Approved  
OMB No. 0704-0188

Public reporting burden for the collection of information is estimated to average 1 hour per response, including the time for reviewing instructions, searching existing data sources, gathering and maintaining the data needed, and completing and reviewing the collection of information. Send comments regarding the burden estimate or any other aspect of this collection of information, including suggestions for reducing the burden, to Washington Headquarters Service, Directorate for Information Operations and Support, 1215 Jefferson Davis Highway, Suite 1200, Arlington, VA 22202-4302, and to the Office of Management and Budget, Paperwork Reduction Project 0704-0188, Washington, DC 20503.

1. AGENCY USE ONLY (Leave Blank)	2. REPORT DATE	3. REPORT TYPE AND DATES COVERED	
	June 1990	Final Feb 89 - Mar 90	
4. TITLE AND SUBTITLE			5. FUNDING NUMBERS
Direct Numerical Simulation of Turbulent Couette Flow (U)			
6. AUTHOR(S)			1L161102AH43
John D. Kuzan and Kurt D. Fickie			
7. PERFORMING ORGANIZATION NAME(S) AND ADDRESS(ES)			8. PERFORMING ORGANIZATION REPORT NUMBER
9. SPONSORING/MONITORING AGENCY NAME(S) AND ADDRESS(ES)			10. SPONSORING/MONITORING AGENCY REPORT NUMBER
Ballistic Research Laboratory ATTN: SLCBR-DD-T Aberdeen Proving Ground, MD 21005-5066			BRL-MR-3838
11. SUPPLEMENTARY NOTES			
12a. DISTRIBUTION/AVAILABILITY STATEMENT			12b. DISTRIBUTION CODE
Approved for public release; distribution is unlimited.			
13. ABSTRACT (Maximum 200 words)			
A direct simulation of fully developed turbulent channel flow with heat transfer has been performed through a direct solution of the time-varying, incompressible, Navier-Stokes equations. Instantaneous streamwise, spanwise, and normal velocity, as well as other turbulence quantities, have been computed. Comparison is made with experimental measurements in the literature. There are discrepancies in the maximum values of the second- through fourth-order statistics. The maximum value of the streamwise turbulence intensity is about ten percent lower than what is found experimentally. The unusually high flatness at the wall suggests that more resolution is required near the wall to sort out the contributions of various sized structures, although calculations with less resolution seem to capture the smallest relevant scales of motion.			
14. SUBJECT TERMS		15. NUMBER OF PAGES	
Projectiles Base Flow		Turbulence Simulation	
39		16. PRICE CODE	
UNCLASSIFIED		17. SECURITY CLASSIFICATION OF REPORT	
UNCLASSIFIED		18. SECURITY CLASSIFICATION OF THIS PAGE	
UNCLASSIFIED		19. SECURITY CLASSIFICATION OF ABSTRACT	
UNCLASSIFIED		20. LIMITATION OF ABSTRACT	
SAR			

**INTENTIONALLY LEFT BLANK.**

## Acknowledgments

John McLaughlin from Clarkson University was the source of the numerical algorithm described in the text. This particular variation of the spectral technique has proven instrumental in successfully attacking the direct simulation problem. Steve Lyons and Thomas Hanratty from the University of Illinois continue to provide their expertise in analyzing the flow fields and suggesting new ways to investigate the results. Jim Danberg and Lann Mann Chang carefully reviewed this work.

Acces... For	
NTIS	CRA&I <input checked="" type="checkbox"/>
DTIC	TAB <input type="checkbox"/>
Unannounced <input type="checkbox"/>	
Justification	
By	
Distribution	
Availability Codes	
Dist	Avail and/or Special
A-1	



**INTENTIONALLY LEFT BLANK.**

# Contents

<b>List of Figures</b>	<b>vii</b>
<b>1 Introduction</b>	<b>1</b>
1.1 Relevance To Aerodynamics and Ballistics . . . . .	1
1.2 The Universal Law of the Wall . . . . .	1
1.3 Turbulent Kinetic Energy . . . . .	3
1.4 The Present Study . . . . .	3
<b>2 Background</b>	<b>4</b>
2.1 Reynolds Decomposition of the Navier-Stokes Equations . . . . .	4
2.2 Channel Flow . . . . .	4
2.3 Viscous Units . . . . .	5
<b>3 A Model of Wall Turbulence</b>	<b>5</b>
<b>4 Governing Equations and Method of Solution</b>	<b>7</b>
4.1 The First Fractional Time Step . . . . .	7
4.2 The Second Fractional Time Step . . . . .	8
4.3 The Third Fractional Time Step . . . . .	8
4.4 The Temperature Field . . . . .	9
4.5 The Spectral Technique . . . . .	9
4.6 The Solution Scheme . . . . .	10
4.7 Other Research . . . . .	11
<b>5 Computational Parameters</b>	<b>11</b>
<b>6 Method of Analysis</b>	<b>13</b>
6.1 General Averages of Turbulence Quantities . . . . .	13
6.2 The Turbulent Energy Budget . . . . .	14
<b>7 Results</b>	<b>15</b>
<b>8 Conclusions</b>	<b>16</b>
<b>Nomenclature</b>	<b>29</b>
<b>References</b>	<b>31</b>
<b>Distribution</b>	<b>33</b>

INTENTIONALLY LEFT BLANK.

## List of Figures

1	Regions in Wall Bounded Flows . . . . .	2
2	Conceptualization of Coupled Near-Wall Structures . . . . .	6
3	Channel Geometry . . . . .	10
4	Velocity . . . . .	18
5	Turbulence Intensity . . . . .	19
6	Expanded View of the Turbulence Intensity . . . . .	20
7	Reynolds Stresses . . . . .	21
8	Turbulence Skewness . . . . .	22
9	Expanded View of the Turbulence Skewness . . . . .	23
10	Turbulence Flatness . . . . .	24
11	Expanded View of the Turbulence Flatness . . . . .	25
12	Turbulent Kinetic Energy Budget . . . . .	26
13	Spanwise-Normal Slice of Flow Field . . . . .	27

INTENTIONALLY LEFT BLANK.

# 1 Introduction

Turbulent flow is the most frequently encountered type of viscous flow, yet a quantitative physical understanding of turbulence remains an unsolved problem. This is true even for the simple case of flow in a straight pipe. We do not know how energy is transferred from the driving force, the pressure gradient, to the turbulent fluid motion. Hence, this simple case provides a starting point for investigations in turbulent flow.

Over the years, many measurements have been made in pipe flows and other wall-bounded flow fields, but the conclusions drawn from the measurements have not been final. While it is possible to measure the instantaneous three components of fluid velocity using laser-Doppler velocimetry, this information provides a very small glimpse of the complete picture. Even with several velocity probes in the flow field and at the wall[1], the picture is incomplete. New experimental techniques, such as pulsed laser velocimetry (which allows planes of instantaneous velocity to be measured), are providing more data about the structure of turbulent wall-bounded flow than any technique to date. None-the-less, an accurate model of the energy transfer process is still lacking.

## 1.1 Relevance To Aerodynamics and Ballistics

Fluid turbulence is important for the computational fluid dynamics solution of the flow field around a projectile in flight. Within this flow field are wall-bounded flows, free shear flows, and wake flows. If the projectile is rocket assisted, has a tracer, or contains a base-burn system, then the flow field may also contain jets. These four distinct types of turbulent flow (free and wall-bounded shear flow, wakes, and jets) span the varieties of fluid turbulence. Each variety has turbulence models, such as mixing length or production-dissipation, that are based on empirical data and require tuning for a specific application. Direct simulation has no such models, but has severe limits in the complexity of the geometry, the size of the Reynolds numbers, and the time required to achieve fully developed turbulent flow.

In spite of the limits, direct simulation provides information that is unavailable from physical experiments, namely the full three-dimensional time-varying flow field. In this way, direct simulation is a "computer experiment" that can be used to tune turbulence models. The long range goal, however, is to develop more complete models for fluid turbulence needed by engineers to compute the mean flow field surrounding a projectile. The steps to this goal include using the direct simulation to obtain a flow field for comparison to large eddy simulation of the small scale motion. This may lead to better understanding and, ultimately, to better models of fluid turbulence.

## 1.2 The Universal Law of the Wall

The early measurements of velocity in wall-bounded flows allowed the construction of the "Universal Law of the Wall" that is depicted in Figure 1. This figure shows that the streamwise fluid velocity component is zero-valued at the wall. Within the "viscous wall

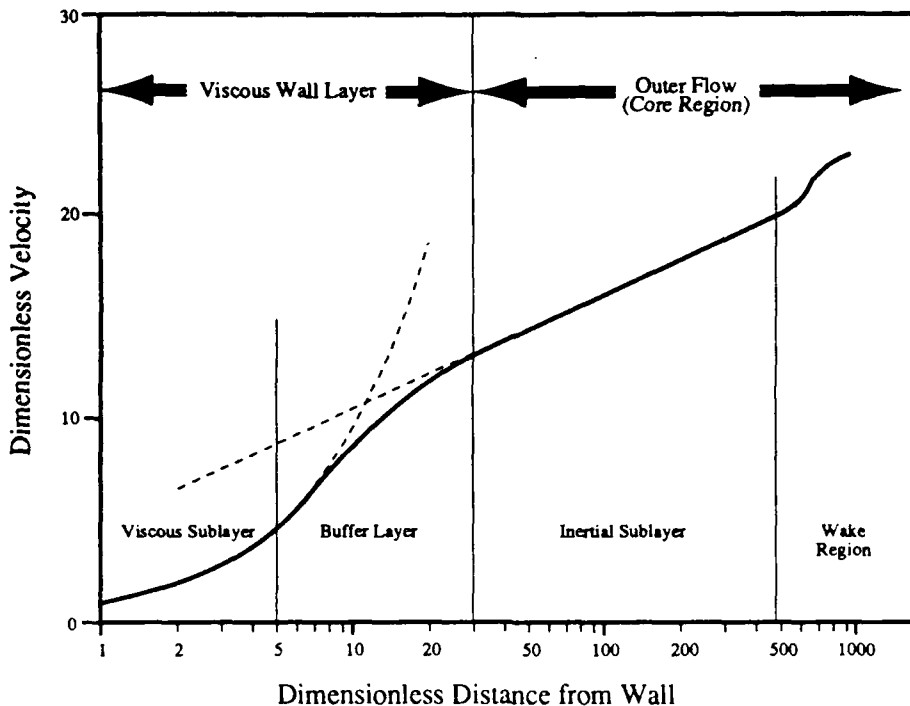


Figure 1: Regions in Wall Bounded Flows

layer" (so called because of the strong effects of viscosity), the velocity increases to a value near that of the time-averaged maximum fluid velocity. The region beyond the viscous wall layer is referred to as the outer flow. As defined in this report, the viscous wall layer contains the viscous (also called laminar or linear) sublayer and the buffer layer, which are commonly mentioned in the literature[2]. The outer flow is sometimes called the core region, and it is a combination of the inertial (or logarithmic) sublayer, and, if present, the wake region[2].

At first, researchers thought that the instability that made a flow become turbulent was to be found mainly in the outer flow. They suggested that the velocity fluctuations found in the outer flow were associated with large eddy structures. These, in turn, fed energy to smaller and smaller eddy structures until, at the wall, the smallest eddy structures transferred the energy to the wall as heat. In this sense, the outer flow controlled the motion of the fluid in the viscous wall layer. The fluid near the wall responded to the velocity fluctuations of the outer flow without influencing the outer flow. This model is not "wrong;" the large eddies do feed the smaller eddies. However, later research showed that the motion of the fluid in the viscous wall layer might have a strong influence on the fluid in the outer flow.

### 1.3 Turbulent Kinetic Energy

At present, the model of fluid turbulence in a wall bounded flow surrounds the two main contributors to the turbulent kinetic energy budget (see Section 6)—the production and dissipation of turbulent kinetic energy. Researchers have found that the production and dissipation do not add to zero in the viscous wall layer; there is extra turbulent kinetic energy available. The result is a supply of turbulent energy to the outer flow, where it is dissipated. Thus, the velocity fluctuations in the outer flow can result from an influx of turbulent kinetic energy from the viscous wall layer. This is a far different notion than the earlier model which suggested that the fluid in the viscous wall layer merely responded to the fluctuations of velocity in the outer flow. Recent measurements show that the viscous wall layer contributes to those fluctuations; in fact, the motion of the fluid in the viscous wall layer may control the motion of the outer flow. The eddies in the viscous wall layer still seem to be influenced by the outer flow. This suggests that there may be a feedback involved in the process. This model, which is far from the final model, is the starting point for the present work.

Currently, the interest is in developing techniques for examining the eddies in the viscous wall layer. Instead of a pipe flow, however, the present study is performed on the flow field between two parallel, flat plates. Thus, the flow field geometry is more closely related to channel flow, although the features of the flow field are quite similar to pipe flow. This paper documents the initial verification that the simulation reproduces nature.

### 1.4 The Present Study

As expected from the periodicity[3] in turbulent flow, Fourier methods arise naturally in the analysis of turbulence and they are exploited in the present study. A direct numerical simulation of turbulent channel flow, using spectral techniques, has been developed[4], and the results are compared to experimental measurements. Since many models exist that predict mean quantities in turbulent channel flow, the most accurate of those models is also discussed as a comparison to the direct simulation.

Research on turbulent fluid flow has been invigorated in the past ten years by the development of supercomputer simulations of flow fields, although direct numerical simulation of turbulent flow in a simple geometry is still a formidable task. The difficulty resides in the wide range of spatial scales; hence, the computational domain must be sized to capture the largest scale of motion while at the same time have small enough grid spacing to resolve the smallest relevant scale. Three dimensional effects must also be considered because of the nonlinear terms in the Navier-Stokes equations,  $\mathbf{v} \cdot \nabla \mathbf{v}$ . These represent the conversion of linear momentum into angular momentum, or the formation of vorticity. To account for vorticity, calculations in three dimensions are required, even for channels where the time-averaged flow is two-dimensional.

## 2 Background

### 2.1 Reynolds Decomposition of the Navier-Stokes Equations

The equations governing the motion of an incompressible fluid are the Navier-Stokes equations:

$$\frac{\partial \mathbf{v}}{\partial t} = -\mathbf{v} \cdot \nabla \mathbf{v} - \frac{1}{\rho} \nabla p + \nu \nabla^2 \mathbf{v} \quad (1)$$

and the continuity equation:

$$\nabla \cdot \mathbf{v} = 0. \quad (2)$$

In these equations,  $\mathbf{v}$  is the instantaneous three dimensional velocity vector,  $t$  is the time,  $\rho$  is the density of the fluid,  $p$  is the hydrodynamic pressure, and  $\nu$  is the kinematic viscosity. Here the coordinate system is Cartesian, and  $(x_1, x_2, x_3)$  are the streamwise, normal, and spanwise directions in the channel geometry with corresponding velocity components  $(v_1, v_2, v_3)$ .

If the instantaneous velocity vector is replaced in Equations 1 and 2 with a velocity vector that is decomposed into a mean flow,  $\mathbf{V}$ , and a fluctuating velocity,  $\tilde{\mathbf{v}}$ , such that:

$$\mathbf{v} = \mathbf{V} + \tilde{\mathbf{v}} \quad (3)$$

then the resulting "Reynolds-decomposed" Navier-Stokes equations contain an additional tensor:

$$\tau_{ij} = -\overline{\rho \tilde{v}_i \tilde{v}_j}. \quad (4)$$

Here,  $\tau_{ij}$  is the Reynolds stress tensor,  $\tilde{v}_i$  and  $\tilde{v}_j$  are the components of the instantaneous velocities, and the overbar represents the time average.

This decomposition into mean flow and turbulent velocity fluctuations isolates the effects of the fluctuations from the mean flow. Now, however, there are nine components of  $\tau_{ij}$  (six are independent) in addition to the  $p$  and the three components of  $\mathbf{V}$ . Herein lies the closure problem of turbulence. While this produces additional stress terms, it does allow solution of the time-averaged Navier-Stokes equations.

One common method of closing the equations is to use the similarity of the form of the Reynolds stress to the viscous stress in the Navier-Stokes equations. An eddy viscosity,  $\nu_t$ , is defined by:

$$\tau_{12} \equiv \rho \nu_t \frac{\partial U(x_2)}{\partial x_2} \quad (5)$$

where  $U(x_2)$  is the streamwise component of the mean velocity.

### 2.2 Channel Flow

The best empirical fit of the velocity profile in a flat-walled channel can be represented by the function for the eddy viscosity developed by Reynolds and Tiederman[5]:

$$\frac{1}{2} + \frac{\nu_t}{\nu} = \frac{1}{2} \sqrt{1 + F^2 G^2} \quad (6)$$

where

$$F \equiv \frac{2}{3} \kappa \left( \frac{x_2}{\nu} \sqrt{\tau_w / \rho} \right) \left( 1 - \frac{x_2}{2h} \right) \left[ 3 - 4 \frac{x_2}{h} + 2 \left( \frac{x_2}{h} \right)^2 \right]$$

and

$$G \equiv \left[ 1 - \exp \left( - \frac{x_2}{\nu A_0} \sqrt{\tau / \rho} \right) \right].$$

In this equation  $h$  is the half-height of the channel,  $\tau$  is the local shear stress,  $\kappa$  is the von Kármán parameter,  $A_0$  is the van Driest parameter, and  $\tau_w$  is the shear stress at the wall defined as:

$$\tau_w \equiv \rho \nu \frac{dU(x_2)}{dx_2} \Big|_{x_2=0}. \quad (7)$$

When this value for the eddy viscosity is substituted into the mixing length model for the Reynolds stress, and that in turn is used in the Reynolds-decomposed Navier-Stokes equations, an excellent approximation to the time-averaged flat-walled channel velocity profile results.

Unfortunately, this result tells us nothing about the dynamics of the flow field; specifically, it does not describe the instantaneous interaction between the wall and the outer flow. Since it is based on empirical data, an experiment is generally required to tune the parameters[6,7,8]. Direct numerical simulation has no such requirement and has the advantage of generating *instantaneous* velocities in three dimensions. This produces a "computer experiment," that can focus other experimental techniques, such as pulsed laser velocimetry[9] and multi-probe hot wire anemometry[1,10,11]. At present, direct numerical simulation is limited to simple geometries and low Reynolds numbers.

### 2.3 Viscous Units

It is convenient to mention viscous units here, which result from making velocity and hydrodynamic pressure dimensionless. This is accomplished with the wall parameters kinematic viscosity,  $\nu$ , and skin-friction velocity,  $v^*$ . Viscous units are denoted by giving the quantity a plus sign superscript.

Thus, hydrodynamic pressure, velocity, and length will be made dimensionless in the following manner:

$$p^+ = \frac{p}{\frac{1}{2} \rho v^*{}^2} \quad v_i^+ = \frac{v_i}{v^*} \quad x_i^+ = \frac{v^*}{\nu} x_i. \quad (8)$$

This allows comparison with experimental results that do not have the same half-height as the channel in the computer experiment.

## 3 A Model of Wall Turbulence

Although the velocity fluctuations in a turbulent flow field are random, coherent structures exist in the viscous wall layer. This was first observed by Beatty, Ferrel and Richardson[12] who showed "streaky structures" that were oriented with the mean flow and repeated

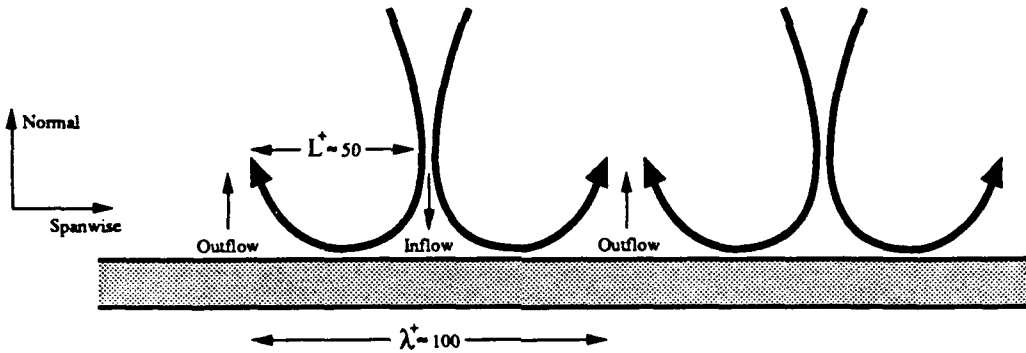


Figure 2: Conceptualization of Coupled Near-Wall Structures

periodically in the direction perpendicular to the mean flow (the spanwise direction in channel flow). These streaky structures, marked with dye or hydrogen bubbles, were found to be regions of low velocity fluid; hence, the fluid had low momentum. The region between the streaky structures contained high momentum fluid.

Streaky structures, marked with dye, traveled downstream and then were lifted away from the viscous wall layer toward the outer flow where they dissipated. This process has been referred to as bursting, and it occurs periodically.

Quantifying bursting and the spacing of streaky structures has been accomplished by many researchers (see Blackwelder and Haritonidis[13]). These quantities are independent of Reynolds number and are found, when made dimensionless with wall parameters, to be  $\lambda^+ \approx 100$  for the spanwise spacing of the streaky structures. The length of a streaky structure is roughly 10 times its width[14]. Further experimental work showed that the streaks were associated with eddies.

In an effort to explain this behavior, Hanratty[14] developed the picture first presented by Townsend[15]. Hanratty suggests that these eddies have inflows and outflows that are of the same strength and that, in a time-averaged sense, the in- and outflows are coupled, as shown in Figure 2. The eddies create streamwise velocity fluctuations by bursting and bringing low momentum fluid from the wall into the outer flow. The opposite is also true; *i.e.*, they carry high momentum fluid toward the wall. High momentum fluid is transported by negative (toward the wall) normal velocities; low momentum fluid is transported by positive normal velocities. Hence, with this transfer process, when the normal velocity is positive, the fluctuating streamwise velocity is negative. This means that both in- and outflows are associated with large values of negative Reynolds shear stress,  $-\bar{v}_1 \bar{v}_2$ .

## 4 Governing Equations and Method of Solution

The Navier-Stokes equations and the continuity equation (Equations 1 and 2) can be rewritten using the following definitions:

$$\boldsymbol{\omega} = \nabla \times \mathbf{v}; \quad \Pi_T = \frac{P}{\rho} + \frac{\tilde{p}}{\rho} + \frac{1}{2} \mathbf{v}^2; \quad \mathbf{v}^2 = \mathbf{v} \cdot \mathbf{v} \quad (9)$$

where  $\boldsymbol{\omega}$  is the vorticity. Term  $\Pi_T$  is the total pressure consisting of the mean,  $P$ , and fluctuating,  $\tilde{p}$ , hydrodynamic pressure and the dynamic pressure. The advection term in the Navier-Stokes equations becomes:

$$\mathbf{v} \cdot \nabla \mathbf{v} = -\mathbf{v} \times \boldsymbol{\omega} + \frac{1}{2} \nabla \mathbf{v}^2 \quad (10)$$

and the Navier-Stokes equations can be written with vorticity explicit:

$$\frac{\partial \mathbf{v}}{\partial t} = \mathbf{v} \times \boldsymbol{\omega} - \nabla \Pi_T + \nu \nabla^2 \mathbf{v}. \quad (11)$$

This form of the equations makes the numerical solution somewhat easier.

### 4.1 The First Fractional Time Step

A three-level fractional step method, developed by Orszag[16], is used to solve the equations. This amounts to setting the left-hand side of Equation 11 equal to each one of the terms on the right-hand side separately (hence, three steps).

By subtracting the mean streamwise hydrodynamic pressure gradient (the mean spanwise and normal gradients are zero) from the second term on the right-hand side of Equation 11 and modeling the streamwise advective term implicitly to reduce convective instability, the advection part of Equation 11 becomes:

$$\frac{\partial \mathbf{v}}{\partial t} + U(x_2) \frac{\partial \mathbf{v}}{\partial x_1} = \mathbf{H} + U(x_2) \frac{\partial \mathbf{v}}{\partial x_1}. \quad (12)$$

where  $U(x_2)$  is the streamwise component of the mean velocity. Function  $\mathbf{H}$  is equal to  $\mathbf{v} \times \boldsymbol{\omega} - \frac{1}{\rho} \frac{dP}{dx_1}$ , where  $\frac{dP}{dx_1}$  is the mean streamwise hydrodynamic pressure gradient. Solving Equation 12 by application of a Crank-Nicholson scheme to the left side and an Adams-Basforth scheme to the right side gives the following result:

$$\frac{\hat{\mathbf{v}}^{n+1} - \mathbf{v}^n}{\Delta t} = \frac{3}{2} \mathbf{H}^n - \frac{1}{2} \mathbf{H}^{n-1} - \frac{1}{2} U(x_2) \left[ \frac{\partial \hat{\mathbf{v}}^{n+1}}{\partial x_1} - 2 \frac{\partial \hat{\mathbf{v}}^n}{\partial x_1} + \frac{\partial \hat{\mathbf{v}}^{n-1}}{\partial x_1} \right], \quad (13)$$

the superscript refers to the time step and the hat (e.g.,  $\hat{\mathbf{v}}$ ) represents quantities resulting after the first fractional time step, also called the “inviscid step.” Solving for  $\hat{\mathbf{v}}^{n+1}$  gives the velocity after the first fractional time step.

## 4.2 The Second Fractional Time Step

The no-penetration boundary condition,  $v_2 = 0$  at the walls, is applied at the second fractional step. An implicit Euler scheme is used which results in:

$$\hat{\mathbf{v}}^{n+1} - \hat{\mathbf{v}}^{n+1} = -\Delta t \nabla \hat{\Pi}^{n+1}. \quad (14)$$

Hence the second step imposes incompressibility and the effects of pressure, and the double hat refers to the velocity after this step. The total pressure ( $\Pi_T$ ) was modified for the first step by subtracting the mean hydrodynamic pressure. Now term  $\Pi$  contains the fluctuating hydrodynamic pressure,  $\tilde{p}$ , and the dynamic pressure so the subscript  $T$  will no longer be used:

$$\Pi = \frac{\tilde{p}}{\rho} + \frac{1}{2} \mathbf{v}^2. \quad (15)$$

The original method of Orszag's did not properly enforce the boundary condition for the pressure field, and continuity was not satisfied at the walls. Using a Green's function method (see Lyons [4]) in this second step corrects the calculated pressure field and satisfies continuity. The pressure term is determined by requiring the divergence of the velocity field to be zero after the second fractional step:

$$\nabla \cdot \hat{\mathbf{v}}^{n+1} = 0. \quad (16)$$

Thus, from 14:

$$\nabla^2 \hat{\Pi}^{n+1} = \frac{\nabla \cdot \hat{\mathbf{v}}^{n+1}}{\Delta t} \quad (17)$$

with the boundary condition:

$$\frac{\partial \hat{\Pi}^{n+1}}{\partial x_2} \Big|_{x_2=0} = \nu \frac{\partial^2 \hat{\mathbf{v}}^{n+1} \cdot \mathbf{j}}{\partial x_2^2} \Big|_{x_2=0}. \quad (18)$$

This is a linear inhomogeneous equation with inhomogeneous boundary conditions. The equation can be split into two parts (an inhomogeneous equation with homogeneous boundary conditions and a homogeneous equation with inhomogeneous boundary conditions). Additionally, the pressure ( $\Pi$ ) is expressed as the sum of an inviscid and a viscous pressure. The viscous part of the pressure satisfies the homogeneous equation, and its boundary conditions are satisfied if and only if continuity is satisfied at the walls. In other words, the inhomogeneous boundary condition is satisfied if and only if Equation 16 is true at the walls. The inviscid part satisfies the inhomogeneous equation, although this does not insure continuity is satisfied.

## 4.3 The Third Fractional Time Step

The final step takes viscosity into account and imposes the no-slip boundary conditions,  $\mathbf{v}^{n+1} = 0$ , at the walls. It is an implicit backward Euler scheme:

$$\mathbf{v}^{n+1} - \hat{\mathbf{v}}^{n+1} = \nu \Delta t \cdot \nabla^2 \mathbf{v}^{n+1}. \quad (19)$$

Non-wall boundary conditions are periodic; the outflow at one “end” is introduced as the inflow at the other “end.” This assumption makes the problem suitable for a Fourier or “spectral” approach. (It is reasonable if the dimensions in the spanwise and streamwise computational domain are more than twice the largest relevant scale of motion in these directions. This information is obtained by experiment, and is discussed below.)

#### 4.4 The Temperature Field

Additionally, a temperature gradient is imposed on the flow field. The walls are held at constant temperatures that are different from each other. The temperature field is then solved in the first and third fractional steps of the computation. The temperature equation is

$$\frac{\partial T}{\partial t} = -\mathbf{v} \cdot \nabla T + \frac{\nu}{\text{Pr}} \nabla^2 T \quad (20)$$

where  $T$  is the temperature and  $\text{Pr}$  is the Prandtl number, which is a ratio of the kinematic viscosity (momentum diffusivity) to the thermal diffusivity. The thermal diffusivity is the ratio of the thermal conductivity to the density and heat capacity.

In order to get homogeneous, Dirichlet boundary conditions the temperature is transformed by

$$T = \theta - Ax_2 \quad (21)$$

where  $\theta$  is the transformed temperature and  $A$  is a constant that controls the temperature difference between the two walls. Following the same procedure as for the convective (first) step of the Navier-Stokes solution scheme, and denoting  $-\mathbf{v} \cdot \nabla \theta - Ax_2$  as  $\mathbf{I}$ , the result is

$$\frac{\hat{\theta}^{n+1} - \theta^n}{\Delta t} = \frac{3}{2} \mathbf{I}^n - \frac{1}{2} \mathbf{I}^{n-1} - \frac{1}{2} U(x_2) \left[ \frac{\partial \hat{\theta}^{n+1}}{\partial x_1} - 2 \frac{\partial \hat{\theta}^n}{\partial x_1} + \frac{\partial \hat{\theta}^{n-1}}{\partial x_1} \right]. \quad (22)$$

The solution scheme is the same as for Equation 13.

Since there is no pressure term in the temperature equation, the remaining terms are solved in the third fractional step as in Equation 19:

$$\theta^{n+1} - \hat{\theta}^{n+1} = \frac{\nu \Delta t}{\text{Pr}} \cdot \nabla^2 \theta^{n+1}, \quad (23)$$

and the boundary conditions are homogeneous.

#### 4.5 The Spectral Technique

Using the spectral method of Orszag[16], the velocity field,  $\mathbf{v} = (v_1, v_2, v_3)$ , can be transformed using the following expansion:

$$\mathbf{v}(\mathbf{x}, t) = \sum_{|l| \leq \frac{L}{2}} \sum_{|m| \leq \frac{M}{2}} \sum_{n=0}^N v_{lmn}(t) \exp \left[ 2\pi i \left( \frac{lx_1}{\lambda_1} + \frac{mx_3}{\lambda_3} \right) \right] T_n \left( \frac{x_2}{h} \right). \quad (24)$$

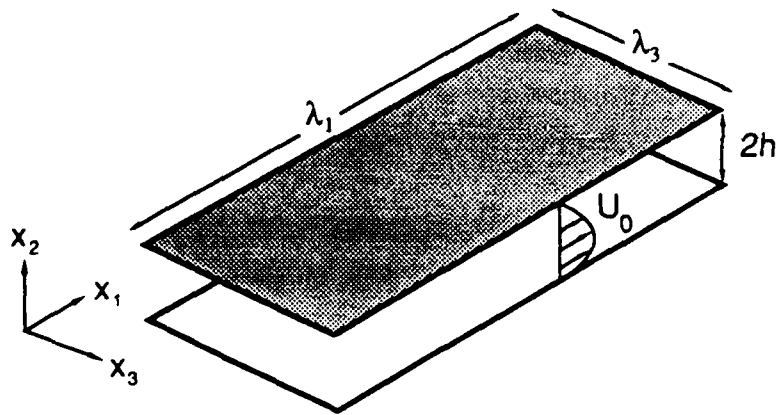


Figure 3: Channel Geometry

In this equation,  $L$  and  $M$  are the number of Fourier modes in the  $x_1$  and  $x_3$  directions,  $T_n$  is a Chebyshev polynomial in the  $x_2$  direction and  $N$  is the degree of the polynomial. Terms  $\lambda_1$  and  $\lambda_3$  are the lengths of the computational domain in the streamwise and spanwise directions, and  $h$  is the channel half-height as shown in Figure 3. The Fourier coefficients of the expansion are represented by  $v_{lmn}(t)$ , and these are referred to collectively as the velocity field in spectral space. The hydrodynamic pressure and the temperature fields are expanded in a similar manner.

This transformation reduces the problem from solving partial differential equations for the velocity, pressure, and temperature fields to solving equations for the spectral coefficients of the physical fields. Spatial derivatives of the velocity field are easily calculated in spectral space; the first derivative of the velocity field in spectral space with respect to the streamwise direction is equal to the the original coefficients multiplied by the factor  $2\pi il/\lambda_1$ . Derivatives with respect to the normal direction are slightly more complicated, but do not require finite differencing and are exact.

The coefficients of the Fourier and Chebyshev series expansions are determined by forcing the series to be an exact representation of the corresponding velocity, temperature, or pressure field at the grid points. A Chebyshev series can be rewritten as a Fourier series; this is used to re-arrange Equation 24 to be the sum of three Fourier series. This allows calculation of the physical space fields by fast Fourier transform—and thus allows calculation of the spectral space coefficients by inverse fast Fourier transform.

#### 4.6 The Solution Scheme

In the solution scheme, the spectral representations of the velocity, temperature, and pressure fields are substituted into the various finite difference equations in the three fractional steps.

In the first fractional step, the terms in function  $H$  are computed in physical space. This is done by transforming the velocity and vorticity fields to physical space via fast Fourier transform, then transforming the resulting " $H$ " field back to spectral space. Also, this procedure is used for the first fractional time step in the temperature field. These terms and the spectral expansions for the velocity and temperature fields are then substituted into Equations 13 and 22.

The second and third fractional steps do not require terms to be calculated in physical space. In these steps, the spectral expansion is substituted into the appropriate finite difference equation and, with some manipulation, the values of the various fields are calculated at the next time step. Since the Navier-Stokes equations describe the motion of the fluid, the dynamics of the flow field are reproduced numerically.

As described, this spectral method produces a finite grid of points with sine waves, representing the velocity, superimposed upon it. These sine waves are multiplied together in the vorticity-velocity cross product of the Navier-Stokes equations, resulting in sums and differences of wavenumbers (inverse wavelength). Longer wavelengths can be resolved on the grid, but the shorter wavelengths can not be resolved and are aliased onto longer wavelengths. (Note that the summations in Equation 24 are centered on zero; hence, infinite wavelength can be resolved but wavenumbers greater than half the number of Fourier modes can not be resolved.) In nature, the energy of the short wavelengths would produce heat, not kinetic energy. To rid the simulation of the short wavelengths, the top third of the wavenumbers in the streamwise and spanwise directions are set to zero before forming the products. This is referred to as "dealiasing." It would appear that half of the wavenumbers should be set to zero in order to dealias, but Orszag[17] has shown that one third is sufficient.

#### 4.7 Other Research

Two other research groups have worked on direct numerical simulation and have developed slightly different solution schemes. Moin and Kim[18] typically have used finite difference schemes in place of the Chebyshev polynomial. Similarly, Kleiser and Schumann[19] use finite differences, although in the solution they employ sequences of one-dimensional scalar Helmholtz equations instead of solving block-tridiagonal matrices.

To date, the results of Moin and Kim[18] and Orszag and Kells[17] appear to reflect turbulent channel measurements the best. Orszag and Kells were more interested in the transition from laminar to turbulent flow; consequently, their algorithm is not suitable for higher Reynolds numbers. The work of Moin and Kim has approximately the resolution of this current study.

### 5 Computational Parameters

In this numerical study, the dimensionless half-height of the channel was 150 viscous units for a Reynolds number of 2260 based on this characteristic length scale (approximately a

pipe Reynolds number of 8,000). The Reynolds number is  $\frac{v_b h}{\nu}$  where  $v_b$  is the bulk velocity, or the integral of the average velocity over the height of the channel. To resolve the large-scale eddies, the spanwise and streamwise dimensions were set at 950 and 1900 viscous units. This produced a bulk velocity of 13.8 in viscous units. The number of spectral modes for the results shown in this paper were  $(L, N, M) = (128, 128, 128)$ .

The Reynolds number determines the largest and smallest scales of motion in the flow field, and it is fixed by the half-height,  $h^+$ . This can be shown by a force balance over the computational domain (see Figure 3). Since, in the spanwise direction, the average velocity is zero and there is no hydrodynamic pressure gradient, the force balance is:

$$2h\lambda_3(P|_1 - P|_2) + \rho h\lambda_3(\overline{\mathbf{v}^2}|_1 - \overline{\mathbf{v}^2}|_2) - 2\lambda_1\lambda_3|\tau_w| = 0. \quad (25)$$

This can be reduced because the average velocity is the same at cross sections 1 and 2, and the hydrodynamic pressure gradient is constant:

$$-\frac{dP^+}{dx_1^+} = \frac{1}{h^+}. \quad (26)$$

Thus picking a half-height determines the mean pressure gradient, which is the driving force. The pressure gradient fixes the Reynolds number since average velocity, kinematic viscosity, and the length scale are fixed.

At this point, the other lengths in the computational domain may be determined. A periodic boundary condition can be used if the computational domain is at least twice the size of the largest periodic structure. The appropriate functions for determining this size are the two-point velocity correlation functions, one in the streamwise direction:

$$R_{ii}(\Delta x_1, 0, 0) = \overline{v_i(x_1, x_2, x_3)v_i(x_1 + \Delta x_1, x_2, x_3)} \quad (27)$$

and a similar function in the spanwise direction. From experimental data[20] the two-point velocity correlation functions vanish at  $3.2h^+$  in the streamwise direction and  $1.6h^+$  in the spanwise direction, while others[18] suggest values of  $6h^+$  and  $3h^+$ . Before vanishing, these two-point velocity correlation functions become negative, and at this spanwise distance distinct streamwise streaks form near the wall in hydrogen bubble experiments[3].

The small scales of motion must also be considered in order to determine the minimum number of grid points or Fourier modes. Relevant scales would begin with the Taylor micro-scale, which fixes the rate of dissipation of turbulent kinetic energy, and increase in size. The smallest scales, the Kolmogoroff scales, are purely dissipative and thus are not important in the direct simulation, although they are crudely represented by dealiasing. Experimental measurements[11] show the Taylor micro-scale to be about 12 viscous units in the spanwise direction and ten times that in the streamwise direction at the wall, where the scales are smallest. Table 1 shows that the Taylor micro-scale may not be resolved at the wall in the spanwise direction for this calculation. Results suggest that this is a minor shortcoming.

Using these values, the size of the computational domain and the grid spacing can be determined. Table 1 shows the resolution available in the current study. The modes were

Direction	Length	Modes	Resolution	Resolvable Scales
Spanwise	950	85	11.18	22.4 to 475
Streamwise	1900	85	22.35	44.7 to 950
Normal	300	128	3.68	.01 to 300
Length, resolution and resolvable scales in viscous units.				

Table 1: Computational Domain Resolution

adjusted for dealiasing. Also, in the normal direction the spacing is stretched toward the channel center so that near the wall, where the smallest scales are present, the resolution is highest.

## 6 Method of Analysis

### 6.1 General Averages of Turbulence Quantities

The solution procedure outlined above generates a computer experiment that is similar to physical experimental facilities, such as water tunnels using particle image velocimetry and laser-Doppler velocimetry. One advantage of the computer experiment is the relative simplicity of obtaining instantaneous, three dimensional velocity measurements at any number of locations, simultaneously, in the flow field.

In the present work the reduction of data that would accompany a physical experiment has been performed, including averages of velocities and moments of velocity. For a physical experiment the averages would be taken either as an ensemble or in time. Thus, at one point in the flow field the mean velocity would be given by:

$$\mathbf{V} = \lim_{t_i \rightarrow \infty} \frac{1}{t_i} \int_{t_0}^{t_0 + t_i} \mathbf{v} dt \quad (28)$$

where  $t_i$  is some elapsed time. A spatial average is used in this work such that a plane of grid points in physical space, parallel to the solid walls, forms the basis of the average. To get higher-order statistics, several planes are averaged together.

Averages of the fluctuating velocities and their moments will be presented. The normal and spanwise mean velocities are zero. The second-order moments are the components of the Reynolds stress, but are also called turbulence intensities. The third- and fourth-order moments are referred to as the skewness ( $\tilde{v}_i \tilde{v}_j \tilde{v}_k$ ) and flatness ( $\tilde{v}_i^2 \tilde{v}_j \tilde{v}_k$ ). Skewness and flatness, involving velocities in two directions, are not well understood, and therefore only  $\tilde{v}_i^3$  and  $\tilde{v}_i^4$  are presented.

## 6.2 The Turbulent Energy Budget

Turbulent energy production and dissipation are also of interest. An equation, commonly called the turbulent kinetic energy budget, that governs the mean kinetic energy,  $\frac{1}{2}\bar{v}_i\bar{v}_i$ , of the turbulent velocity fluctuations can be obtained from the Navier-Stokes equations. Multiplying Equation 1 by the fluctuating velocity, taking the time average, and subtracting the mean kinetic energy budget gives:

$$V_j \frac{\partial}{\partial x_j} \left( \frac{1}{2} \bar{v}_i \bar{v}_i \right) = -\bar{v}_i \bar{v}_j S_{ij} - \frac{\partial}{\partial x_j} \left( \frac{1}{2} \bar{v}_i \bar{v}_i \bar{v}_j + \frac{1}{\rho} \bar{v}_i \bar{p} - 2\nu \bar{s}_{ij} \bar{s}_{ij} \right) - 2\nu \bar{s}_{ij} \bar{s}_{ij}. \quad (29)$$

The mean strain rate,  $S_{ij}$ , and the strain-rate fluctuations,  $\bar{s}_{ij}$ , are the symmetric parts of the mean and fluctuating deformation rates. The total deformation rate is

$$\frac{\partial v_i}{\partial x_j} = s_{ij} + r_{ij} \equiv \frac{1}{2} \left( \frac{\partial v_i}{\partial x_j} + \frac{\partial v_j}{\partial x_i} \right) + \frac{1}{2} \left( \frac{\partial v_i}{\partial x_j} - \frac{\partial v_j}{\partial x_i} \right) \quad (30)$$

and the mean and fluctuating rates are similarly defined.

Equation 29 shows that the rate of change of the turbulent kinetic energy is due to two kinds of deformation work and three forms of transport. If the energy flux in a control volume is zero, two of the transport terms (the second and third terms on the right-hand side) redistribute the energy from one location to another. The pressure gradient-velocity interaction (the first term on the right-hand side) arises from pressure fluctuations. In an incompressible fluid the contribution of the mean pressure to the deformation work is zero, but the fluctuating pressure contributes to the turbulent kinetic energy. Thus, the first two terms represent the interaction of the velocity with the sum of the fluctuating hydrodynamic pressure and the dynamic pressure.

Deformation-work terms, the last two terms on the right-hand side, represent turbulence production and viscous dissipation. Turbulence production describes the exchange of kinetic energy between the mean flow and the fluctuations. Viscous dissipation is the rate at which viscous stresses perform deformation work against the fluctuating strain rate. These terms are of interest in an instantaneous sense, too, as described in the introduction.

For plane channel flow, Equation 29 may be written as:

$$0 = -\bar{v}_1^+ \bar{v}_2^+ \frac{dV_1^+}{dx_2^+} - \frac{\partial}{\partial x_2^+} \left( \frac{1}{2} \bar{v}_1^+ \bar{v}_1^+ \bar{v}_2^+ \right) - \frac{\partial \bar{p}^+ \bar{v}_2^+}{\partial x_2^+} + \frac{\partial^2}{\partial x_2^{+2}} \left( \frac{1}{2} \bar{v}_1^+ \bar{v}_1^+ \right) - \left( \frac{\partial \bar{v}_1^+}{\partial x_2^+} \right)^2. \quad (31)$$

The five terms on the right side of this equation are the production, turbulent transport, fluctuating pressure gradient-velocity interaction transport, rate of viscous diffusion, and the isotropic dissipation of turbulent kinetic energy, respectively. They are hereafter denoted as  $\mathcal{P}$ ,  $\mathcal{T}$ ,  $\mathcal{G}$ ,  $\mathcal{V}$ , and  $\mathcal{D}$ , respectively. In this more specific case, terms  $\mathcal{T}$  and  $\mathcal{G}$  are

associated with only the normal velocity fluctuations, and term  $\mathcal{V}$  is affected only by the change in the normal direction. Term  $\mathcal{P}$  is reduced to the Reynolds shear stress interaction with the mean flow velocity gradient, and this is the major source for turbulent kinetic energy. This shows the importance of the Reynolds shear stress. Since term  $\mathcal{D}$  is isotropic (in its expansion, there are nine terms), it remains unchanged. This term is important when near the wall; far from the wall its contribution is almost zero. Its role is to transport turbulent kinetic energy to the wall, where it is dissipated.

## 7 Results

The initial flow field was laminar with small random fluctuations in two dimensions (zero divergence determines the third component). The calculation was allowed to run until the average streamwise velocity profile settled down to steady, fully developed turbulent flow. At the grid dimensions mentioned above this took about 300 hours of Cray 2 time.

The computed velocity results are shown in Figure 4. They are compared with the hot wire anemometer data of Eckelman[21] and the laser-Doppler velocimetry measurements of Niederschultze[22]. If the data were plotted with semi-logarithmic scales, a “logarithmic” layer would be present in the data of Eckelman, but not in the other two sets of data. This is due to the low Reynolds number of the latter sets of data (roughly a value of 2200), while the data of Eckelman are at a Reynolds number of 5600. The “logarithmic” layer (see Figure 1) appears at a Reynolds number of about 4000.

Turbulence intensity profiles are shown in Figure 5 and Figure 6. Another second-order statistic profile, the Reynolds shear stress, is shown in Figure 7. The streamwise turbulence intensity is compared to Eckelman and to Niederschultze; note the maximum in the center of the shear layer near the wall at a distance of 12 viscous units. The normal and spanwise profiles are similar, although the maxima are not as pronounced. Good agreement exists between the computed data and the experimental data, although the maxima are slightly less for the computed data. Hot wire anemometer data are typically high when measuring values in the directions perpendicular to the bulk velocity, as shown in the figures. The discrepancy in the spanwise maximum can not be explained.

Skewness and flatness profiles are shown in the next four figures; the results are as expected. Note that they are significantly different from the Gaussian value of zero (for skewness) and three (for flatness), although this is the same behavior as that found by Niederschultze. The values of the flatness near the wall are somewhat large, when compared to the experimental data. Even with laser velocimetry, third- and fourth-order statistics are difficult to measure close to the wall. However, the high value of the flatness in the streamwise direction suggests that the simulation does not match nature in this respect. Note that the spanwise skewness and the normal flatness approach their Gaussian values in the outer flow.

Figure 12 is the total turbulent kinetic energy budget, as described by Equation 31. Since the normal and spanwise contributions to the total turbulent kinetic energy budget are very small when compared to the streamwise component, the total budget is very

similar to the streamwise budget. The terms identified on the figure are those described in Section 6. Unfortunately, there are no experimental data to compare with; however, the values are very similar to predictions made from pure shear flows and extrapolated to channels[2]. As explained in the introduction, the production and dissipation of turbulent kinetic energy (curves  $\mathcal{P}$  and  $\mathcal{D}$ ) are such that the transport of kinetic energy is away from the viscous wall layer. This is shown in the Figure 12; the transport terms appear as negative quantities.

Figure 13 shows a spanwise-normal "slice" of the instantaneous velocities in the spanwise and normal directions. Each velocity vector originates from one of the grid points in the solution scheme (the grid points are in a rectangular array). Along the walls ( $x_2=0$  or 300) there are several eddies, which appear as circular masses of vectors, as well as the associated in- and outflows that are shown schematically in Figure 2. Note the outflow at  $x_2=0$  near  $x_3=750$  and the inflow near  $x_3=300$ ; these eddies are about the size (50 units) that would produce the spacing of the streaky structures discussed in Section 3. In- and outflows do not appear to be spaced every 100 units in this slice. Future work will involve averaging techniques to examine the near-wall turbulent structure.

Although the temperature gradient was included in the calculations, there are no significant results to be presented. When vector plots are made on color-graphics terminals, the transport of heat can be seen. This ability to track other transport properties of the flow field may be of interest in future work.

## 8 Conclusions

A direct numerical simulation of turbulent flow has been compared with experimental results. The computed averaged quantities agreed closely with those values obtained in the laboratory. There are discrepancies in the maximum values of the second- through fourth-order statistics. The maximum value of the streamwise turbulence intensity is about ten percent lower than what is found experimentally. Since the experimental data are considered very accurate, the numerical simulation is flawed in this respect. It is possible that the streamwise length of the computational domain is not large enough and structures that should have died out are re-introduced to the flow field. This would have the effect of extending the correlation length, which in turn would lower the absolute values of the zero-separation correlation, or the turbulence intensity. Since the computed turbulence intensity matches the experimental values in the normal direction (for the laser velocimetry data), the streamwise values are even more suspect. Currently, efforts are directed to increasing the computational length in the streamwise direction by a factor of two, while maintaining the same resolution. These results should be available for the next report.

Similar arguments hold for the skewness and flatness, although the experimental data for these statistics are not as reliable as the second-order moments. The unusually high flatness at the wall suggests that more resolution is required near the wall to sort out the contributions of various sized structures, although calculations with less resolution seem to capture the smallest relevant scales.

Future direction for this computer simulation involves investigation of the eddies in the viscous wall region. This work will center around some type of averaging technique. There are many techniques that are used to find structures in wall bounded flow fields[23]. Unfortunately, many of these techniques are akin to counting wheels on vehicles passing by on a street corner: The average number is three, but not one tricycle rode past. An averaging technique that allows counting events that are found instantaneously is needed, instead of a technique that results in an average structure that may have no resemblance to the instantaneous flow field at all.

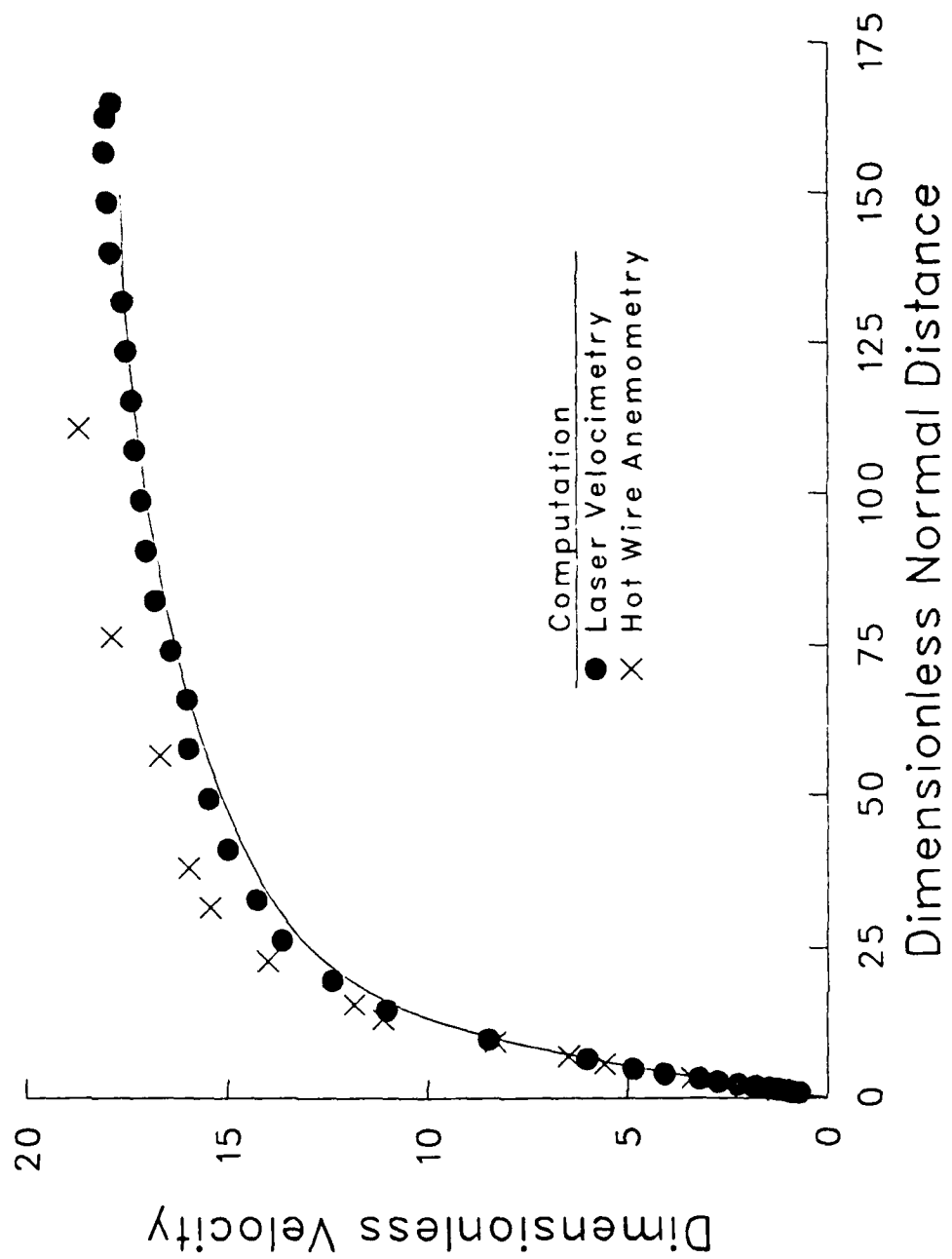


Figure 4: Velocity

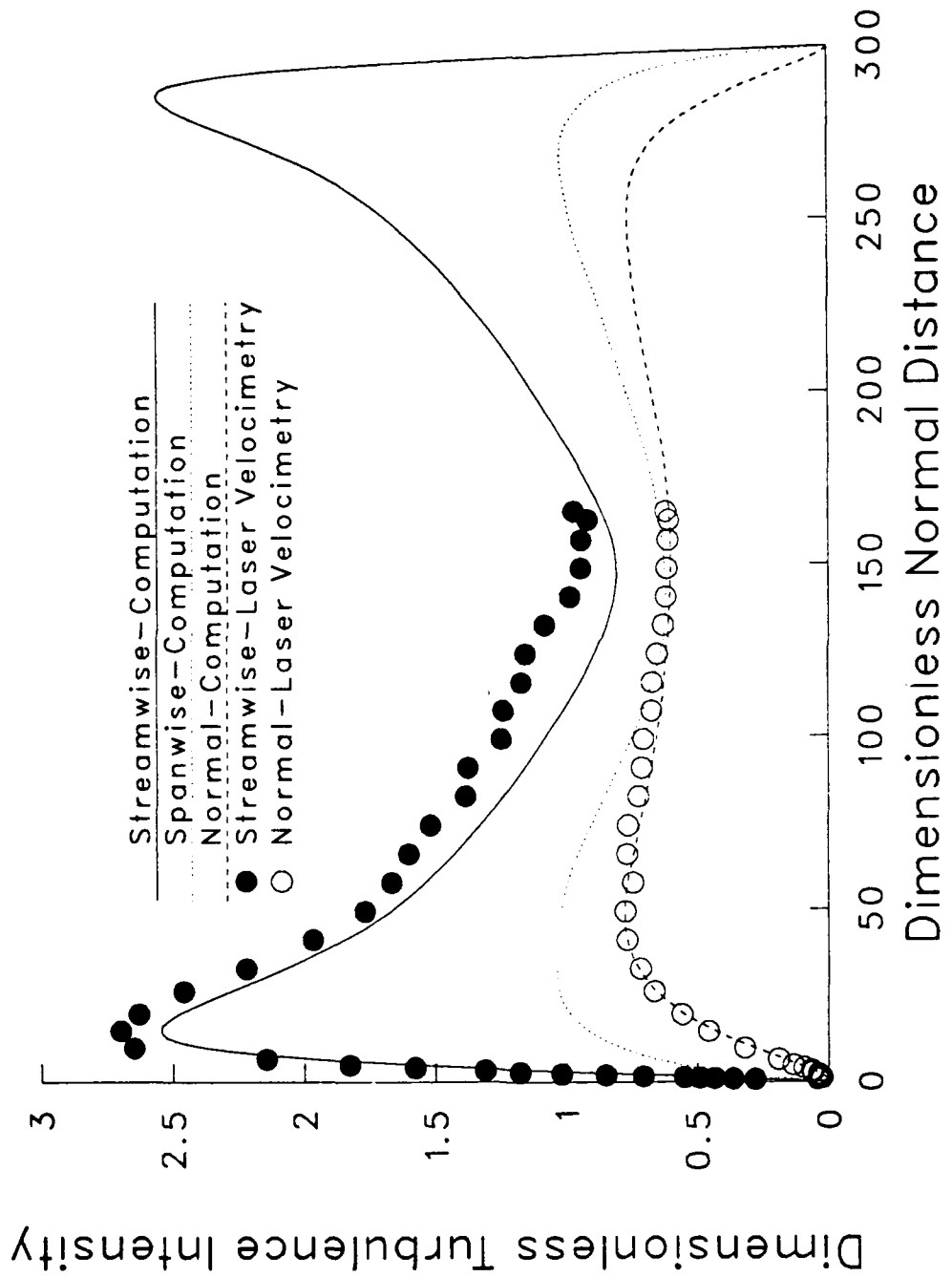


Figure 5: Turbulence Intensity

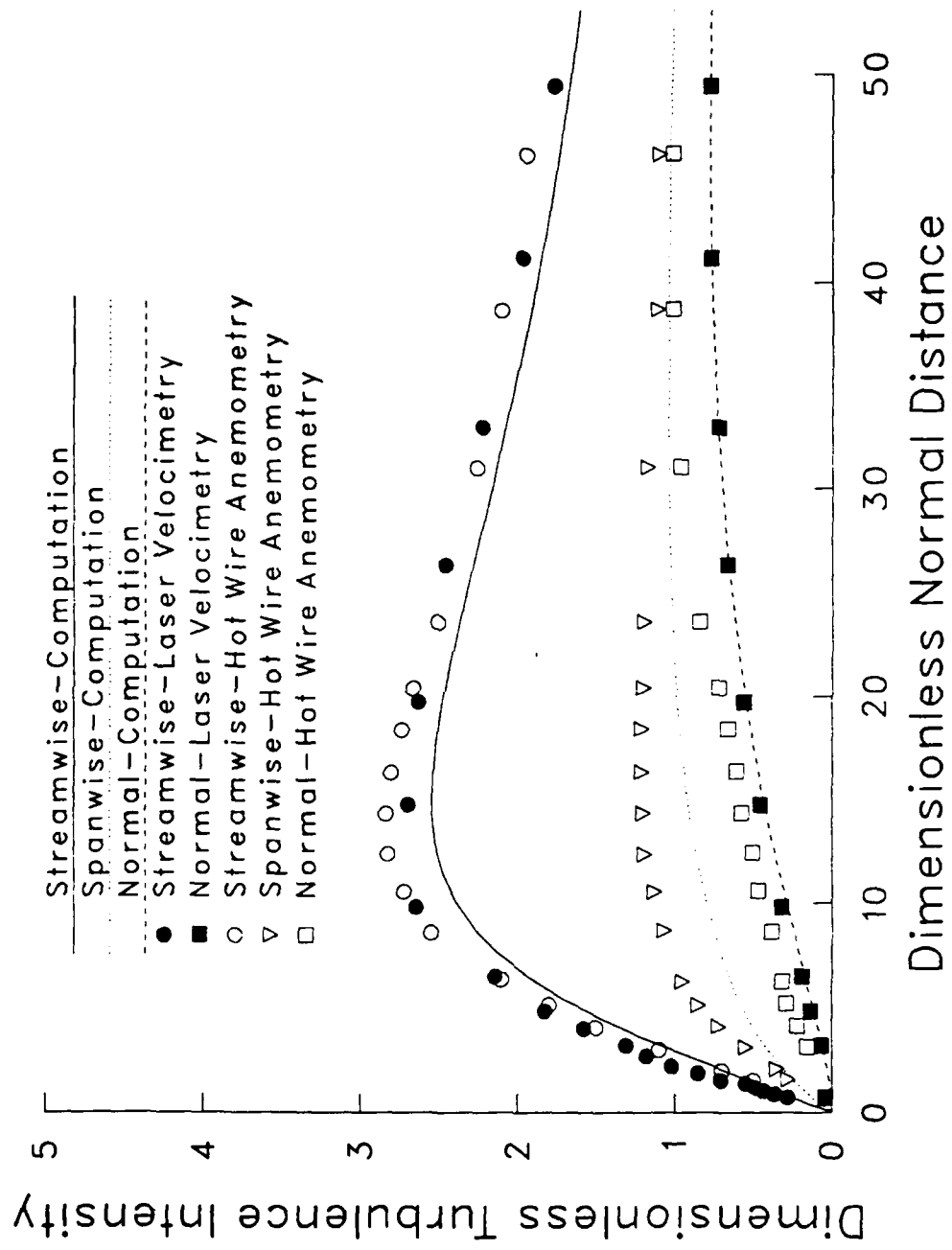


Figure 6: Expanded View of the Turbulence Intensity

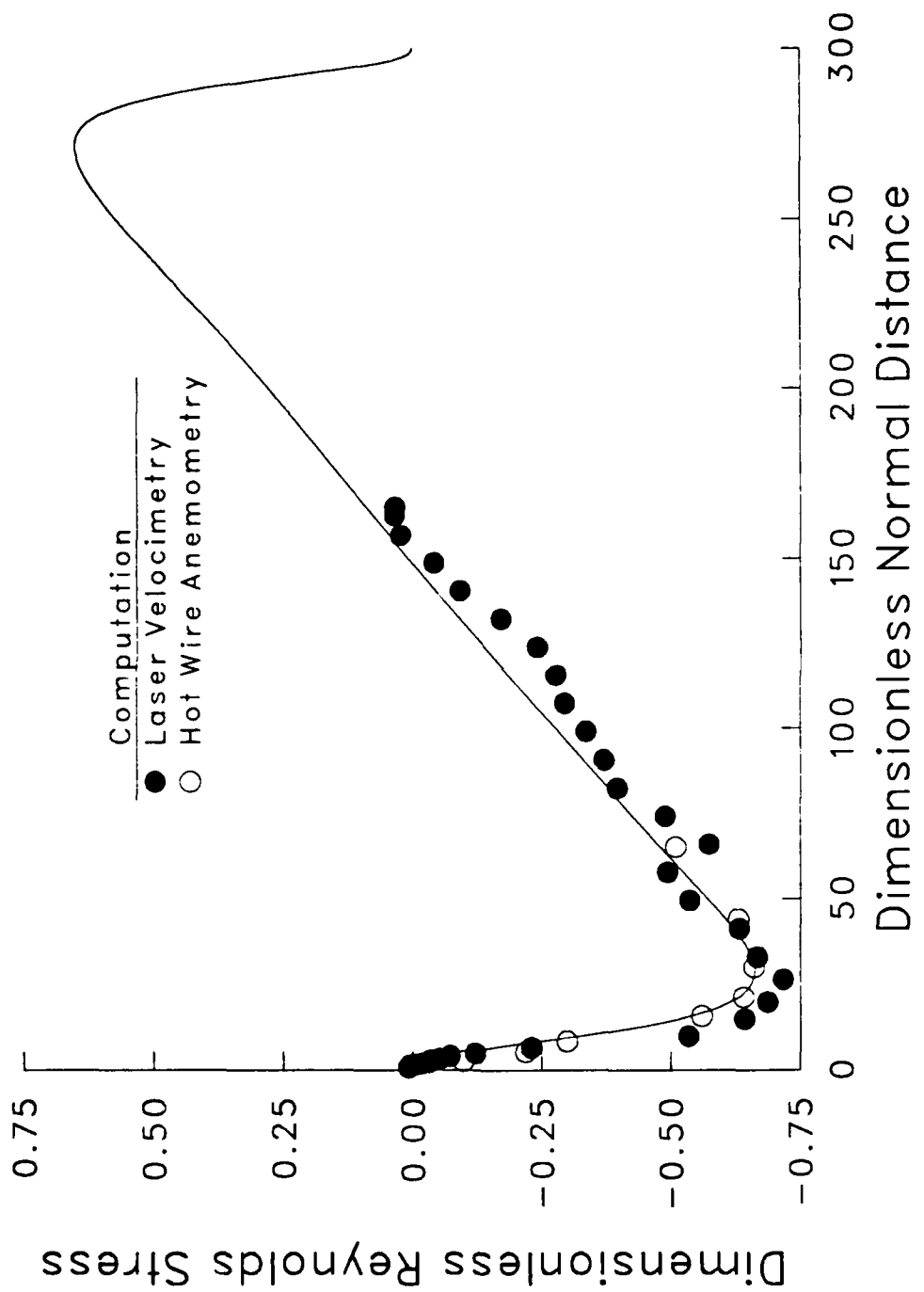


Figure 7: Reynolds Stresses

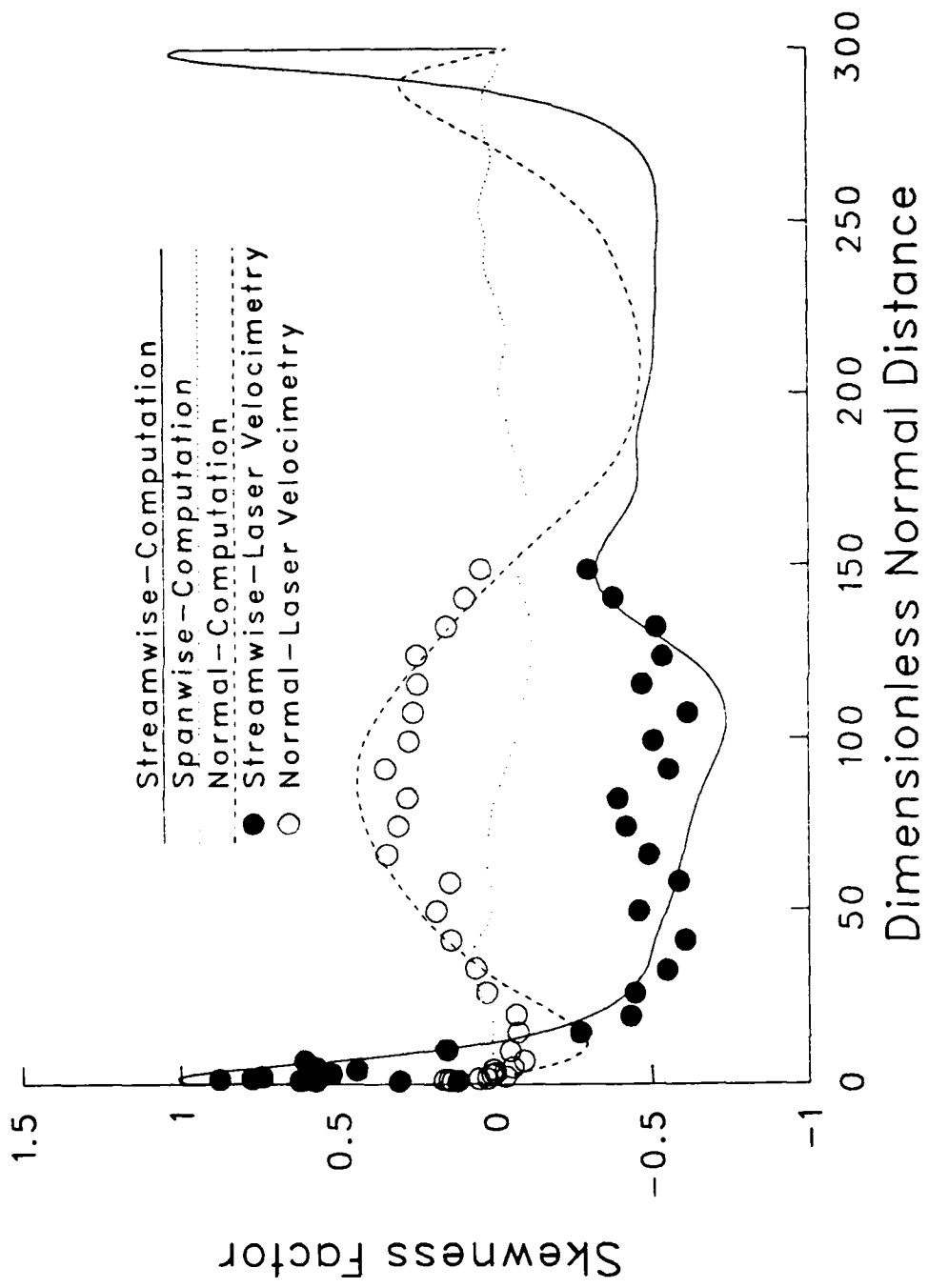


Figure 8: Skewness Factor

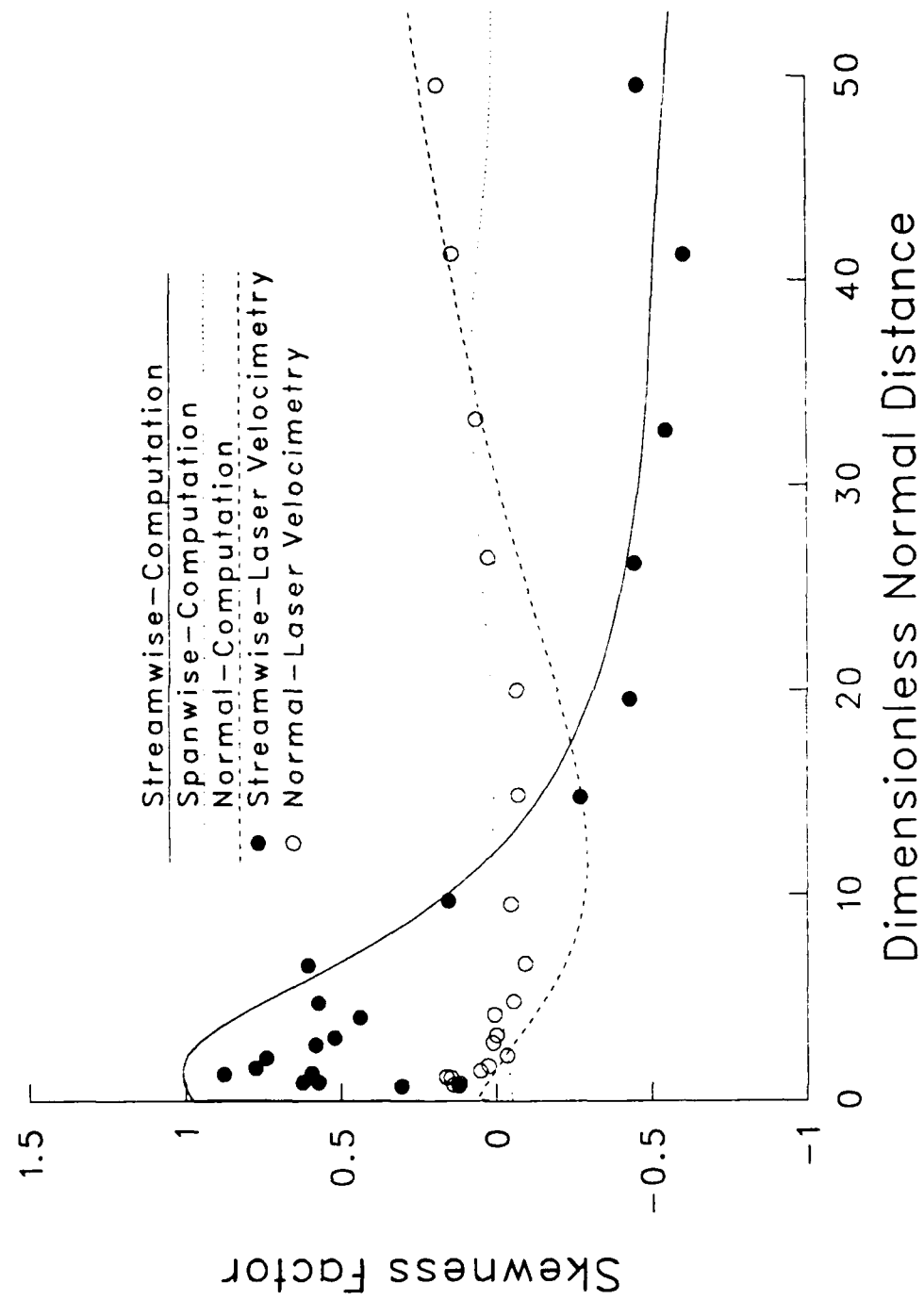


Figure 9: Expanded View of the Skewness Factor

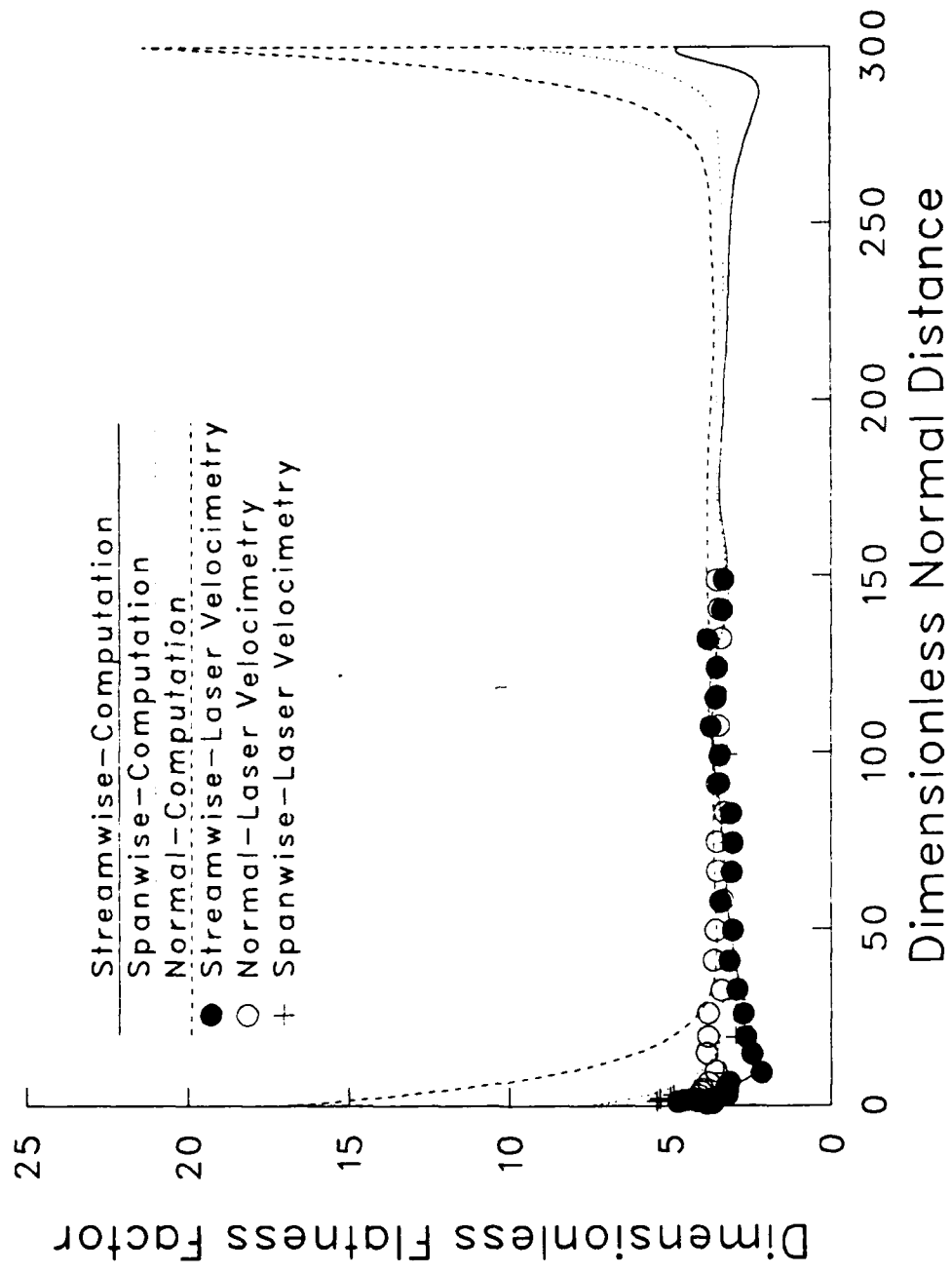


Figure 10: Flatness Factor

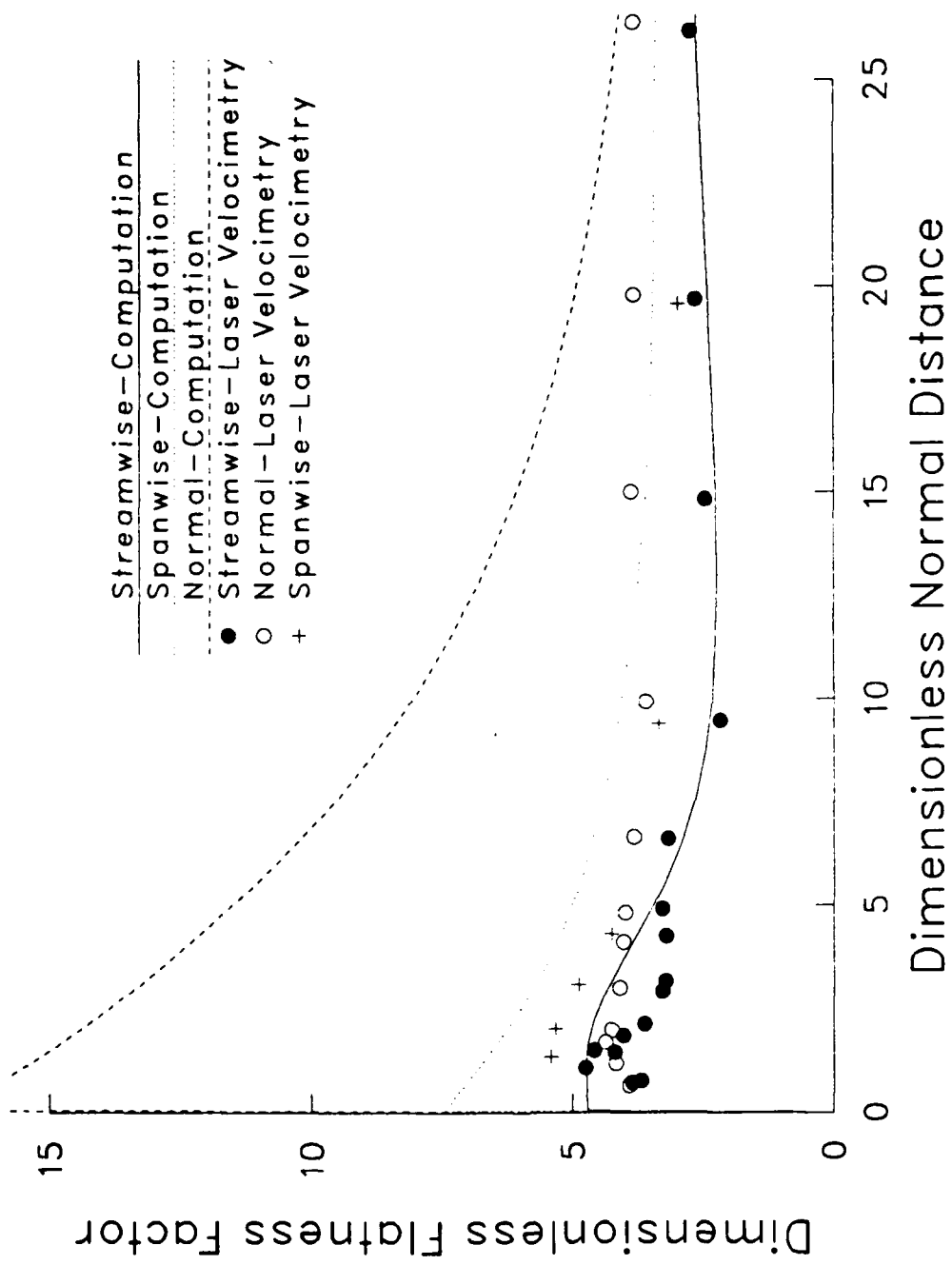


Figure 11: Expanded View of the Flatness Factor

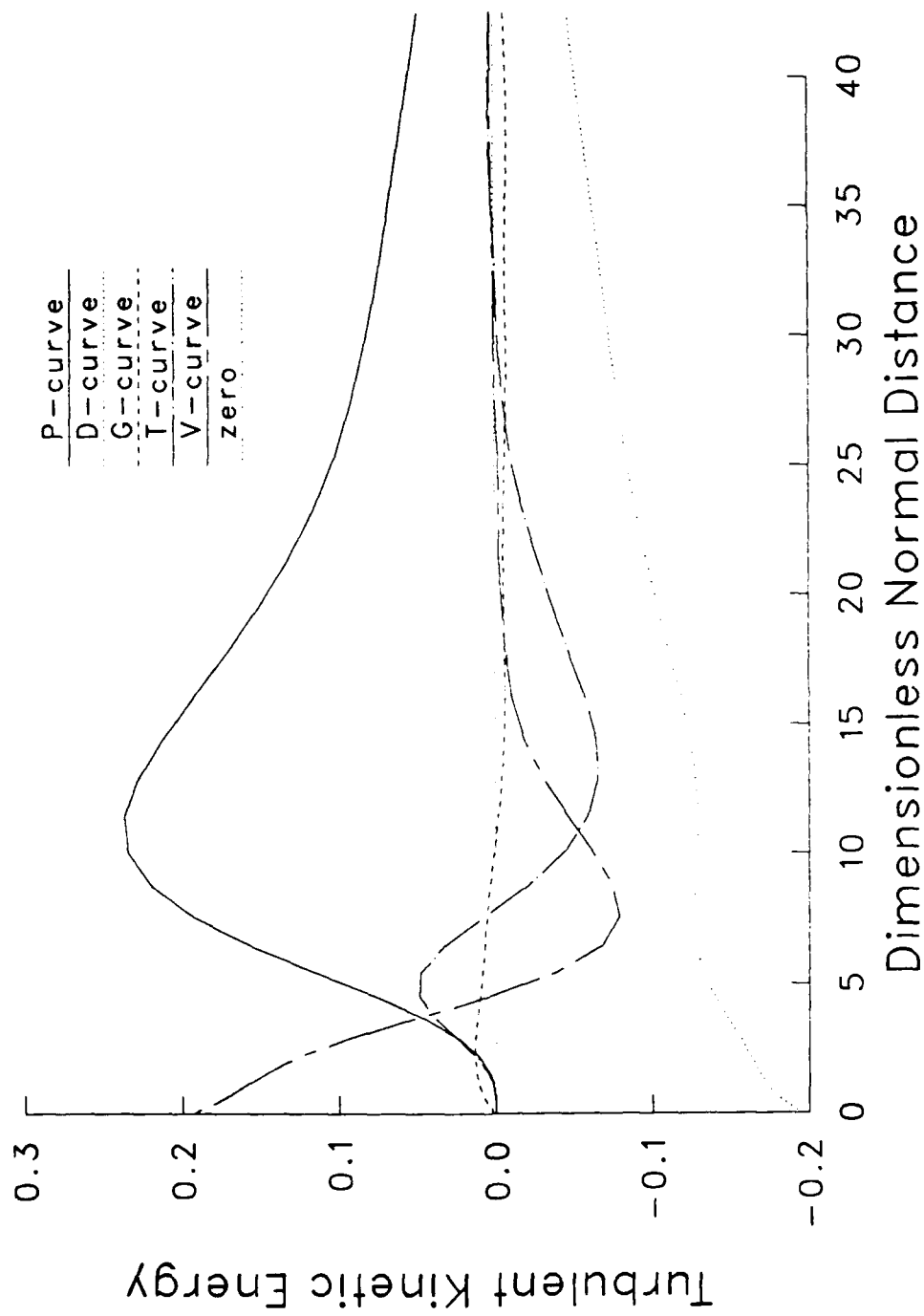


Figure 12: Turbulent Kinetic Energy Budget

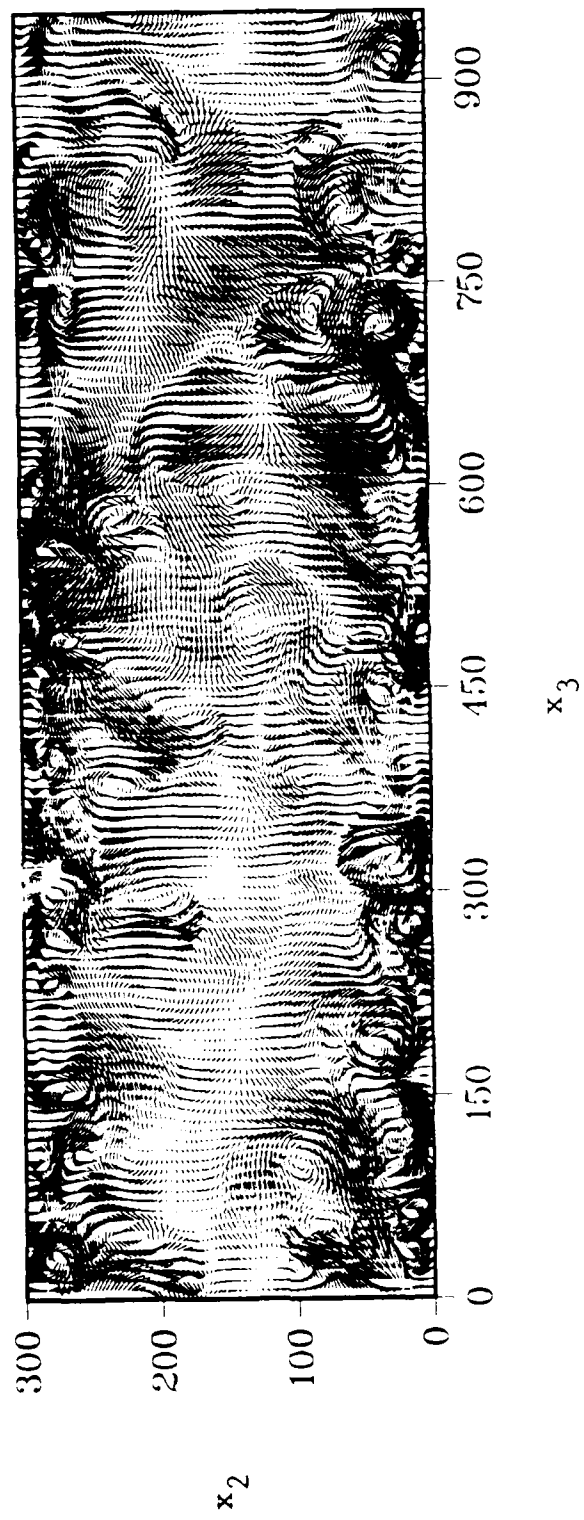


Figure 13: Instantaneous Spanwise-Normal Slice of the Flow Field

INTENTIONALLY LEFT BLANK.

## Nomenclature

The general system of nomenclature followed in this report is as follows:

1. A bold face symbol represents a three-dimensional vector quantity.
2. A subscript of 1, 2, or 3 represents the value of a quantity in a particular direction where:
  - (a) Number 1 represents the streamwise direction
  - (b) Number 2 represents the normal direction
  - (c) Number 3 represents the spanwise direction.
3. A subscript of  $i$  or  $j$  is used for indicial notation of vector quantities and second degree tensor quantities when  $i$  and  $j$  appear together.
4. An overbar denotes a time average.
5. A tilde denotes a fluctuating quantity (see Equation 3).
6. A plus sign superscript denotes a dimensionless quantity (see Equation 8).
7. Upper-case represents the mean quantity.

### Lower-case Symbols

Symbol	Meaning
$h$	Channel half-height
$p$	Hydrodynamic pressure
$t$	Time
$v$	Velocity
$v^*$	Skin-friction velocity
$x$	Direction in the computational domain

### Upper-case Symbols

Symbol	Meaning
$A$	Constant for temperature equation
$A_0$	The van Driest parameter
$L$	Number of Fourier modes in the streamwise direction
$M$	Number of Fourier modes in the spanwise direction
$N$	Degree of the Chebyshev polynomial (normal direction)
$R_{ij}$	Strain rate
$S_{ij}$	Strain rate
$T$	Temperature
$T_B^+$	Time between “bursts”
$U(x_2)$	Streamwise component of the mean velocity
Re	Reynolds number
Pr	Prandlt number

### Greek Symbols

Symbol	Meaning
$\kappa$	The von Kármán parameter
$\lambda$	Length of the computational domain
$\lambda^+$	Spanwise spacing of the streaky structures
$\nu$	Kinematic viscosity
$\nu_t$	Eddy viscosity
$\rho$	Density
$\tau$	Local shear stress
$\tau_{ij}$	Reynolds stress tensor
$\tau_w$	Wall shear stress
$\theta$	Transformed temperature
$\omega$	Vorticity
$\Pi$	Modified total pressure
$\Pi_T$	Total pressure

## References

- [1] M. Lee. Near-wall measurements in turbulent channel flow. Ph.D. Thesis, Department of Chemical Engineering, University of Illinois, Urbana, 1975.
- [2] H. Tennekes and J. L. Lumley. *A First Course in Turbulence*. MIT Press, London, 1972.
- [3] K. Nishino N. Kasagi, M. Hirata. *Streamwise Pseudo-Vortical Structures and Associated Vorticity in the Near-Wall Region of a Wall-Bounded Turbulent Shear Flow*. 9th Symp. Turbulence, Rolla, Missouri, 1984.
- [4] S. L. Lyons. A direct numerical simulation of fully developed turbulent channel flow with passive heat transfer. Ph.D. Thesis, Department of Chemical Engineering, University of Illinois, Urbana, 1989.
- [5] W.C. Reynolds and W.G. Tiederman. Stability of turbulent channel flow, with application to Malkus's theory. *J. Fluid Mech.*, 27:252-272, 1967.
- [6] K.A. Frederick. Velocity measurements for turbulent nonseparated flow over solid waves. Ph.D. Thesis, Department of Chemical Engineering, University of Illinois, Urbana, 1986.
- [7] J.D. Kuzan. Separated flow over a large amplitude wavy surface. M.S. Thesis, Department of Chemical Engineering, University of Illinois, Urbana, 1983.
- [8] J.W. McLean. Computation of turbulent flow over a moving wavy boundary. *Phys. Fluids*, 1983. 26, 2065-2073.
- [9] R. J. Adrian and C. S. Yao. Development of pulsed laser velocimetry for measurement of turbulent flow. Proceedings of Symposium on Turbulence in Liquids, University of Missouri, Rolla, 1984.
- [10] H. Schlichting. *Boundary Layer Theory, 4th edition*. McGraw Hill, New York, 1960.
- [11] D. S. Finnicum. Measurements of the taylor micro-scale in turbulent pipe flow. *Physics of Fluids*, 28:1654-1669, 1985.
- [12] S. Corsin. Symposium on naval hydrodynamics. *Publication Number 515, National Academy of Science*, 373-415, March 1956.
- [13] R. F. Blackwelder and J. H. Haritonidis. Scaling of bursting phenomenon. *Structure and Mechanisms of Turbulence, Lecture Notes in Physics*, 75-87, January 1978.
- [14] T. J. Hanratty. A conceptual model of the viscous wall region. In *Near Wall Turbulence*. Hemisphere Publishing Co., Washington, DC, 1989.
- [15] A. A. Townsend. *The Sturcture of Turbulent Shear Flow*. Cambridge University Press, Cambridge, 1976.
- [16] S. Orszag. Numerical simulations of incompressible flows within simple boundaries: accuracy. *J. Fluid Mech.*, 49:75-112, 1971.
- [17] S.A. Orszag and L.C. Kells. Transition to turbulence in plane poiseuille flow and plane couette flow. *J. Fluid Mech.*, 99:159-205, 1980.

- [18] P. Moin and J. Kim. On the numerical solution of time-dependent viscous incompressible fluid flows involving solid boundaries. *J. Comput. Phys.*, 35:381-392, 1980.
- [19] L. Kleiser and U. Schumann. Treatment of incompressibility and boundary conditions in 3-d numerical spectral simulations of plane channel flow. Proc. 3rd GAMM Conf. on Numerical Meth. in Fluid Mech., 1980. 165-173.
- [20] G. Compte-Bellot. Écoulement turbulent entre deux parois parallèles. Ph.D. Thesis, University of Grenoble, France, 1963.
- [21] H. Eckelman and H. Reichardt. An experimental investigation in a turbulent channel flow with a thick viscous sublayer. Proceedings of Symposium on Turbulence in Liquids, University of Missouri, Rolla, 1971.
- [22] M.S. Niederschultze. Velocity and pressure measurements in turbulent channel flow. Ph.D. Thesis, Department of Chemical Engineering, University of Illinois, Urbana, 1988.
- [23] S. K. Robinson, S. J. Kline, and P. R. Spalart. Quasi-coherent structures in the turbulent boundary layer. *Zoran P. Zarić Memorial International Seminar on Near-Wall Turbulence*, 1-35, May 1988.

<u>No of Copies</u>	<u>Organization</u>	<u>No of Copies</u>	<u>Organization</u>
1	Office of the Secretary of Defense OUSD(A) Director, Live Fire Testing ATTN: James F. O'Bryon Washington, DC 20301-3110	1	Director US Army Aviation Research and Technology Activity Ames Research Center Moffett Field, CA 94035-1099
2	Administrator Defense Technical Info Center ATTN: DTIC-DDA Cameron Station Alexandria, VA 22304-6145	1	Commander US Army Missile Command ATTN: AMSMI-RD-CS-R (DOC) Redstone Arsenal, AL 35898-5010
1	HQDA (SARD-TR) WASH DC 20310-0001	1	Commander US Army Tank-Automotive Command ATTN: AMSTA-TSL (Technical Library) Warren, MI 48397-5000
1	Commander US Army Materiel Command ATTN: AMCDRA-ST 5001 Eisenhower Avenue Alexandria, VA 22333-0001	1	Director US Army TRADOC Analysis Command ATTN: ATAA-SL White Sands Missile Range, NM 88002-5502
1	Commander US Army Laboratory Command ATTN: AMSLC-DL Adelphi, MD 20783-1145	(Class. only) 1	Commandant US Army Infantry School ATTN: ATSH-CD (Security Mgr.) Fort Benning, GA 31905-5660
2	Commander US Army, ARDEC ATTN: SMCAR-IMI-I Picatinny Arsenal, NJ 07806-5000	(Unclass. only) 1	Commandant US Army Infantry School ATTN: ATSH-CD-CSO-OR Fort Benning, GA 31905-5660
2	Commander US Army, ARDEC ATTN: SMCAR-TDC Picatinny Arsenal, NJ 07806-5000	1	Air Force Armament Laboratory ATTN: AFATL/DLODL Eglin AFB, FL 32542-5000
1	Director Benet Weapons Laboratory US Army, ARDEC ATTN: SMCAR-CCB-TL Watervliet, NY 12189-4050		<u>Aberdeen Proving Ground</u>
1	Commander US Army Armament, Munitions and Chemical Command ATTN: SMCAR-ESP-L Rock Island, IL 61299-5000	2	Dir, USAMSAA ATTN: AMXSY-D AMXSY-MP, H. Cohen
1	Commander US Army Aviation Systems Command ATTN: AMSAV-DACL 4300 Goodfellow Blvd. St. Louis, MO 63120-1798	1	Cdr, USATECOM ATTN: AMSTE-TD
		3	Cdr, CRDEC, AMCCOM ATTN: SMCCR-RSP-A SMCCR-MU SMCCR-MSI
		1	Dir, VLAMO ATTN: AMSLC-VL-D

No. of  
Copies Organization

2 Commander  
US Army, ARDEC  
ATTN: SMCAR-AET-A,  
R. Kline  
H. Hudgins  
Picatinny Arsenal, NJ 07806-5000

1 Commander  
US Army Missile Command  
ATTN: AMSMI-RDK, W. Dahlke  
Redstone Arsenal, AL 35898-5010

1 Commander  
Naval Surface Warfare Center  
ATTN: Dr. W. Yanta  
Aerodynamics Branch  
K-24, Building 402-12  
White Oak Laboratory  
Silver Spring, MD 20910

1 Arizona State University  
Department of Mechanical and  
Energy Systems Engineering  
ATTN: Dr. G. P. Neitzel  
Tempe, AZ 85281

## USER EVALUATION SHEET/CHANGE OF ADDRESS

This Laboratory undertakes a continuing effort to improve the quality of the reports it publishes. Your comments/answers to the items/questions below will aid us in our efforts.

1. BRL Report Number BRL-MR-3848 Date of Report Jun 90
2. Date Report Received \_\_\_\_\_
3. Does this report satisfy a need? (Comment on purpose, related project, or other area of interest for which the report will be used.)  
\_\_\_\_\_  
\_\_\_\_\_
4. Specifically, how is the report being used? (Information source, design data, procedure, source of ideas, etc.)  
\_\_\_\_\_  
\_\_\_\_\_
5. Has the information in this report led to any quantitative savings as far as man-hours or dollars saved, operating costs avoided, or efficiencies achieved, etc? If so, please elaborate.  
\_\_\_\_\_  
\_\_\_\_\_
6. General Comments. What do you think should be changed to improve future reports? (Indicate changes to organization, technical content, format, etc.)  
\_\_\_\_\_  
\_\_\_\_\_

**CURRENT ADDRESS**

Name \_\_\_\_\_  
Organization \_\_\_\_\_  
Address \_\_\_\_\_  
City, State, Zip Code \_\_\_\_\_

7. If indicating a Change of Address or Address Correction, please provide the New or Correct Address in Block 6 above and the Old or Incorrect address below.

**OLD ADDRESS**

Name \_\_\_\_\_  
Organization \_\_\_\_\_  
Address \_\_\_\_\_  
City, State, Zip Code \_\_\_\_\_

(Remove this sheet, fold as indicated, staple or tape closed, and mail.)

-----  
FOLD HERE-----

**DEPARTMENT OF THE ARMY**

Director

U.S. Army Ballistic Research Laboratory

ATTN: SLCBR-DD-T

Aberdeen Proving Ground, MD 21005-5066

**OFFICIAL BUSINESS**



NO POSTAGE  
NECESSARY  
IF MAILED  
IN THE  
UNITED STATES

**BUSINESS REPLY MAIL**  
FIRST CLASS PERMIT No 0001, APG, MD

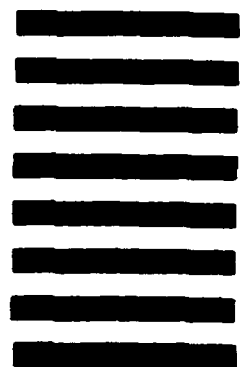
POSTAGE WILL BE PAID BY ADDRESSEE

Director

U.S. Army Ballistic Research Laboratory

ATTN: SLCBR-DD-T

Aberdeen Proving Ground, MD 21005-9989



-----  
FOLD HERE-----